dented rate constants for interprotein ET, but also reveals details of the conformational distributions and dynamics that underlie protein-protein binding and reaction.

References and Notes

1. R. E. Blankenship, *Molecular Mechanisms of Photosynthesis* (Blackwell Science, Oxford, ed. 1, 2002).
2. V. L. Davidson, *Acc. Chem. Res.* **41**, 730 (2008).
3. M. Prudêncio, M. Ubbink, *J. Mol. Recognit.* **17**, 524 (2004).
4. C. C. Page, C. C. Moser, P. L. Dutton, *Curr. Opin. Chem. Biol.* **7**, 551 (2003).
5. H. B. Gray, J. R. Winkler, *Proc. Natl. Acad. Sci. U.S.A.* **102**, 3534 (2005).
6. J. M. Nocek, A. K. Knutson, P. Xiong, N. Petlakh Co, B. M. Hoffman, *J. Am. Chem. Soc.* **132**, 6165 (2010).
7. See supporting materials on *Science* Online.
8. J. M. Nocek, B. P. Sishta, J. C. Cameron, A. G. Mauk, B. M. Hoffman, *J. Am. Chem. Soc.* **119**, 2146 (1997).
9. S. Papp, J. M. Vanderkooi, C. S. Owen, G. R. Holtom, C. M. Phillips, *Biophys. J.* **58**, 177 (1990).
10. D. N. Beratan et al., *Acc. Chem. Res.* **42**, 1669 (2009).
11. M. N. Berberan-Santos, E. N. Bodunov, B. Valeur, *Chem. Phys.* **315**, 171 (2005).
12. D. Lukoyanov, B. M. Barney, D. R. Dean, L. C. Seefeldt, B. M. Hoffman, *Proc. Natl. Acad. Sci. U.S.A.* **104**, 1451 (2007).
13. J. M. Nocek et al., *J. Am. Chem. Soc.* **113**, 6822 (1991).
14. J. R. Winkler, B. G. Malmström, H. B. Gray, *Biophys. Chem.* **54**, 199 (1995).
15. M. M. Ivković-Jensen et al., *Biochemistry* **38**, 1589 (1999).
16. L. Geren, B. Durham, F. Millett, *Methods Enzymol.* **456**, 507 (2009).
17. X.-M. Gong, M. L. Paddock, M. Y. Okamura, *Biochemistry* **42**, 14492 (2003).
18. W. Zinth, J. Wachtveitl, *ChemPhysChem* **6**, 871 (2005).
19. Funding for this work was provided as follows: P.X., J.M.N., and B.M.H., the National Institute of Health (grant HL063203); J.V.-W., J.V.L., and M.R.W., as part of the ANSER Center, an Energy Frontier Research Center funded by U.S. Department of Energy, Office of Science, Office of Basic Energy Sciences (DE-SC0001059).

Zooming In on Microscopic Flow by Remotely Detected MRI

Vikram S. Bajaj,* Jeffrey Paulsen, Elad Harel,† Alexander Pines*

Magnetic resonance imaging (MRI) can elucidate the interior structure of an optically opaque object in unparalleled detail but is ultimately limited by the need to enclose the object within a detection coil; acquiring the image with increasingly smaller pixels reduces the sensitivity, because each pixel occupies a proportionately smaller fraction of the detector's volume. We developed a technique that overcomes this limitation by means of remotely detected MRI. Images of fluids flowing in channel assemblies are encoded into the phase and intensity of the constituent molecules' nuclear magnetic resonance signals and then decoded by a volume-matched detector after the fluids flow out of the sample. In combination with compressive sampling, we thus obtain microscopic images of flow and velocity distributions ~10^6 times faster than is possible with conventional MRI on this hardware. Our results illustrate the facile integration of MRI with microfluidic assays and suggest generalizations to other systems involving microscopic flow.

In the hospital and laboratory alike, magnetic resonance imaging (MRI) routinely provides detailed information about the structure, fluid dynamics, and chemistry deep within opaque objects, organs, and materials. However, the conventional geometry of an MRI experiment severely limits its sensitivity for a ubiquitous class of applications, including cerebrovascular angiography and parallel microfluidic assays, in which the dimensions of the imaged objects are orders of magnitude larger than those of the fluid-containing channels they enclose. Because the signal in an inductive nuclear magnetic resonance (NMR) coil is proportional to the magnetic flux the coil encloses, the sensitivity of an NMR detector is optimized when the feature of interest completely fills the detector's active volume—a constraint that cannot be met for these systems. In addition, local magnetic field gradients at the interface of fluid and solid channel boundaries cause line broadening and exacerbate this loss of sensitivity. Both fac-

tors severely limit the accessible resolution—the ability to zoom in to see details of interest—in the MRI of microfluidic devices, porous materials, or biological fluid channels in the brain and other organs.

To sensitively image a microscopic feature of a flowing system, an NMR coil should ideally be embedded within the object such that it precisely encloses only the element of interest. Indeed, this approach has been adopted in microfluidic device studies: Multiple radio frequency–resonant structures have been fabricated directly on a chip, such that each detector is matched to the dimensions of the microchannel that fills it (*1–4*). However, this method will not easily scale to circuitous or highly parallel microfluidic geometries because it requires a separate and isolated resonant circuit and electronics for each detector in the array (*2, 5*), and it additionally obscures the correlation between elements in the flow pathway. It cannot be integrated into existing microfluidic assays, nor can it be applied to microporous materials (*6*), microchromatography columns, or living systems, whose internal fluid channels are inherently inaccessible to a local detector.

We have developed a suitable alternative to this direct mode of NMR detection. Remote detection (*7*) is a generalization of multidimensional NMR (*8*) in which physical translation of the sam-

ple occurs before acquisition of the signal (see fig. S1). We have applied remote detection to gas flow in channels (*9*) and porous materials (*10*) and to time-resolved liquid flow (*11*). Here, we introduce a combination of methods that allow us to zoom in on the microscopic details of microfluidic flow dynamics in three spatial dimensions via the amplifying action of remote flow. These methods include fabrication of microsolenoid NMR probes with demountable microfluidic device holders; design of remote MRI sequences for spatial encoding in the presence of motion, as well as for velocimetric measurements; and compressive sampling algorithms for faster image encoding. This combination of remote MRI methods (Fig. 1) spectroscopically mimics the implantation of a coil around a microscopic feature of interest. The mechanism of remote detection is analogous to that of a magnetic recording tape on which complex data are first encoded and later read out by a single stationary detector as the tape advances.

Specifically, the macroscopic imaged structure (e.g., microfluidic chip) is enclosed by a conventional MRI coil, which we use only to encode information in the phase of the NMR signal of any analyte (solute or solvent) containing spin-½ nuclei, such as protons. We can use any Fourier phase-encoding pulse sequence without modification from the library of conventional MRI methods to encode the desired spatial, dynamic (*12–14*), or chemical information (fig. S3). However, instead of inefficiently detecting the result with the same coil, we next store the NMR phase information as long-lived longitudinal magnetization (intensity) that decays with the spin lattice relaxation time, which is usually several seconds for diamagnetic fluids such as water or organic solvents (fig. S4). Within that time, the encoded fluid flows to a detector whose volume is matched to the feature of interest (e.g., microfluidic channel), where the information encoded within it—a spectrum or an image—is read out as the fluid flows past. Our method does not require the encoded fluid packets to arrive at the detector in order; simple Fourier transformation yields both the encoded information and a correlated time-of-flight dimension that reflects the arrival of fluid packets at the detector. Most important, because

Materials Sciences Division, Lawrence Berkeley National Laboratory, Berkeley, CA 94720, USA, and Department of Chemistry, University of California, Berkeley, CA 94720, USA.

*To whom correspondence should be addressed. E-mail: vsbajaj@lbl.gov (V.S.B.); pines@berkeley.edu (A.P.)
†Present address: James Franck Institute, University of Chicago, Chicago, IL 60637, USA.

the volume of our single detector is matched to the size of the interesting features, remote detection allows us to zoom in on them while minimizing the sensitivity loss due to filling factor or susceptibility broadening. This setup provides a signal enhancement of 400 relative to conventional MRI for our geometry and in the experiments we present here (Figs. 2 and 3).

Further, because the Fourier image coefficients are stored and then read out indirectly, we benefit from tremendous flexibility in the way that they are digitally sampled. Indeed, most systems for which remote detection is likely to be useful are sparse in that their interesting features occupy a small fraction of the image field of view. Just as sparse electronic data can be compressed to a fraction of their normal volume, our images can be represented and sampled sparsely. Sparse or nonuniform sampling of the Fourier space is critically important in reducing the time required to acquire images with high resolution and high dimensionality. This is because a conventional MRI image comprises repetitions of an experiment whose parameters are serially incremented to encode each point in the multidimensional Fourier space. Its acquisition therefore requires a time proportional to the product of the number of points in each dimension. By using compressed

sensing, now also introduced in clinical MRI (15), we further reduce acquisition times in remotely detected images by factors of 8 to 64 by sampling only a chosen subset of these points. Our implementation of compressed sensing relies on the sparse representation of images in the wavelet domain (16) and nonlinear reconstruction (fig. S5) (17). Combining sparse sampling with remote detection allows us to record images about 1 million times as quickly as in a conventional MRI experiment that might be recorded using the same imaging hardware [enhancement by a factor of ~1100 to 3200 gives $\sim 1000^2 = 10^6$ increase in speed (17)].

In the examples below, we enclose microfluidic devices (chip dimensions ~3 cm by 4 cm; microfluidic channels with rectangular cross section of 50 to 150 μm) with a commercially produced volume-encoding coil (40 mm × 40 mm cylinder) in an unmodified high-field MRI system. We subject them to magnetic field gradients (Fig. 1) that encode information about the spatial distribution of flow and its velocity in the spin degrees of freedom of water, although the method is generically applicable to any analyte. Our detector is a microsolenoid (250 μm × 0.5 mm) NMR probe connected to the outlet of the microfluidic device. We acquire NMR signals stroboscopically as the detector coil empties and fills

with new encoded fluid. Accordingly, our scheme (Fig. 1B) uses gradient pulses that compensate for the deleterious effects of fluid motion during the encoding period or render the signal phase sensitive to the velocity alone while removing its dependence on position and acceleration (13, 18) [hereafter called phase contrast (17)].

We thus explore the limits of resolution at commercially available gradient strengths, achieving a time resolution of 30 ms and spatial resolution of better than 15 μm, at flow rates approaching 100 cm/s. These measurements furthermore explicitly correlate two complementary descriptions of the flow field—the Lagrangian, in which the flow is parameterized in terms of fluid parcel trajectories and times of flight, and the Eulerian, in which the velocity is specified at each point in space—in three spatial dimensions. By contrast, optical measurements in the en face geometry typically require transparent samples and confocal arrangements to image concentration or velocity gradients in the perpendicular dimension. Our method, however, resolves only the components of the velocity field that are in steady state over the duration of the experiment; non–steady-state flow contributes a random phase and cannot be elucidated using this or other MRI-based techniques.

To validate our method, we applied remotely detected velocimetry to three microscale structures: a microcapillary (diameter 50 μm), a serpentine microfluidic mixer, and a constricted microchannel. In the first case, it is well known that the pressure-driven flow of water should produce a parabolic axial velocity profile due to the vanishing relative velocity of viscous liquids at solid boundaries. This expected distribution is indeed revealed by two-dimensional sections of axial velocity–encoded images (Fig. 2, A and B). These high-resolution (15 μm) experiments also illustrate several unique features of remotely detected velocimetry. Beyond revealing expected correlations between time of flight and local velocity, the data demonstrate how the image appearance depends predictably on this time of flight to the detector, in the sense that faster-moving components arrive at earlier times of flight. Further, because the velocity varies continuously, each voxel contains a distribution of velocities that are measured as a geometric average in phase contrast measurements, but are separated here by a Lagrangian time-of-flight parameter (fig. S3). Alternatively, the true velocity distribution can also be measured by Fourier velocity methods (see below), in which the velocity-encoding gradient is stepped through a series of values to generate a conjugate Fourier dimension that encodes the velocity distribution.

Next, we applied our velocimetry method to flow in a serpentine microfluidic mixer (Fig. 2 and movies S1 and S2), in which the encoded transverse velocity, orthogonal to the overall axis of flow, changes in sign as the channel winds back and forth. Finally, we investigated flow in a constricted microchannel—an important geometry
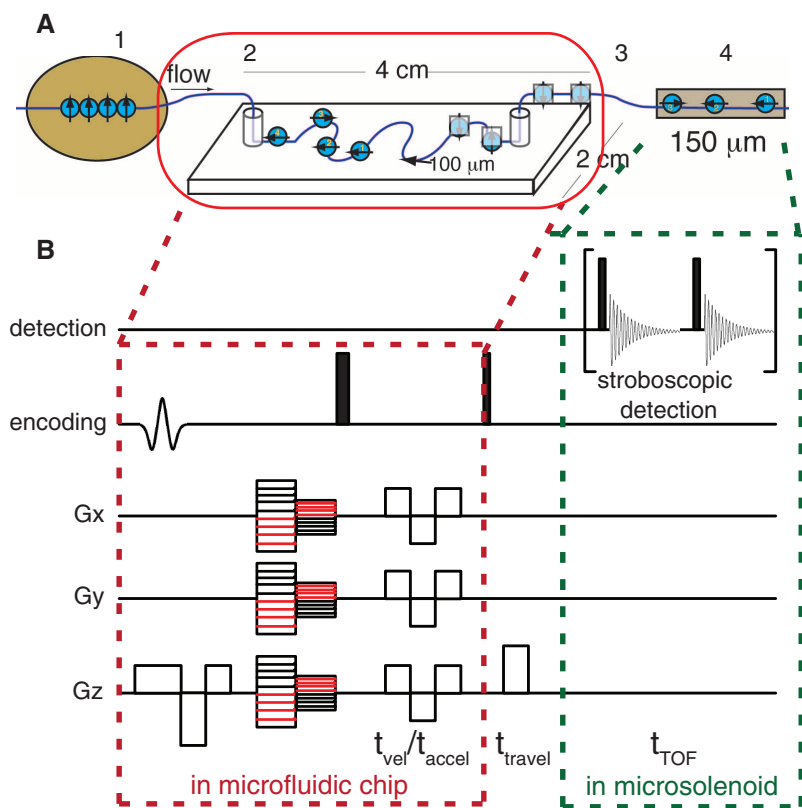

Fig. 1. Remotely detected MRI. (**A**) Spins in fluid analytes are polarized (1) in an MRI magnet and then encoded (2) in an MRI volume coil with switchable gradients (encircled in red). Information is stored (3) as the fluid travels to an optimized microsolenoid detector (4), where it is detected (still in the MRI magnet). (**B**) MRI pulse sequence. After slice selection, information is encoded into the phase of the NMR signal by magnetic field gradients (Gx, Gy, Gz) and stored by a π/2 pulse for travel to the detector, where it is detected stroboscopically. t_{vel} and t_{accel}, times over which velocity- or acceleration-phase encoding is performed; t_{travel}, travel time from chip to microsolenoid; t_{TOF}, time for travel of a fluid packet from chip to detector.

because many microfluidic elements, including valves and connectors, incorporate discontinuous changes in the channel boundary. We examined accelerating water flow through the constriction with 20-μm resolution (first using conventional, not compressed, sampling to validate the method). The data in Fig. 3A and movie S3 clearly resolve both the faster components of the flow and those that are retarded by the constriction and arrive later. Further, multidimensional velocity images with three spatial dimensions (Fig. 3B), acquired with compressed sensing, illustrate that flow near the constriction appears dispersive at this spatial resolution. Indeed, fine Fourier sampling of the velocity dimension (Fig. 3C) reveals a broad velocity distribution for voxels near the constriction, and, because these measurements simultaneously elucidate flow in the Lagrangian picture, the time-of-flight dispersion curves (Fig. 3D) for spins that transit this voxel similarly reveal correlated information about the dispersion.

Our approach thus addresses two important problems in microfluidics. Microfluidics promises to miniaturize laboratory-scale chemistry so that it can be conducted in parallel and in portable devices (19–22). However, critically lacking for the design of new devices (as well as for parallel assays in existing ones) is a nonperturbing tool to probe both microscale chemistry and flow dynamics (23). Although NMR spectra contain specific chemical information and MRI delivers information about flow distributions, neither is generically suitable for microfluidic applications in its conventional incarnation (24). Remote detection is a method by which a single generic NMR-MRI detector can easily be coupled to any microfluidic geometry without modification. Nonetheless, microfluidic remote detection has a number of limitations. It is applicable only to analytes that are themselves NMR-active or can be detected indirectly by contrast agents or other sensors. Moreover, the residence time of the analytes in the device after encoding must be less than that required for the spins to relax to thermal equilibrium polarization (T_1 relaxation). For example, if a remotely detected microfluidic assay requires an incubation period longer than T_1, it will have to be conducted first with the flow arrested, to be followed by MRI encoding of the result and transport to the remote detector within a time shorter than T_1.

This method also has potential applications beyond microfluidics. Microsolenoid NMR detectors routinely achieve picomolar mass sensitivity (1). Thus, without specialized hardware, our method can now be applied to flow in microporous materials and, with detection of chemical shifts (11), to high-throughput studies of combinatorial chemistry, cellular metabolism, and small-molecule screening. Next, its application to analogous flow structures in vivo may enable sensitive localized spectroscopy—and possibly imaging—of microvasculature in the brain, kidneys, and liver with catheter microcoils or surface coil detectors and blood as the encoding fluid, particularly if slowly
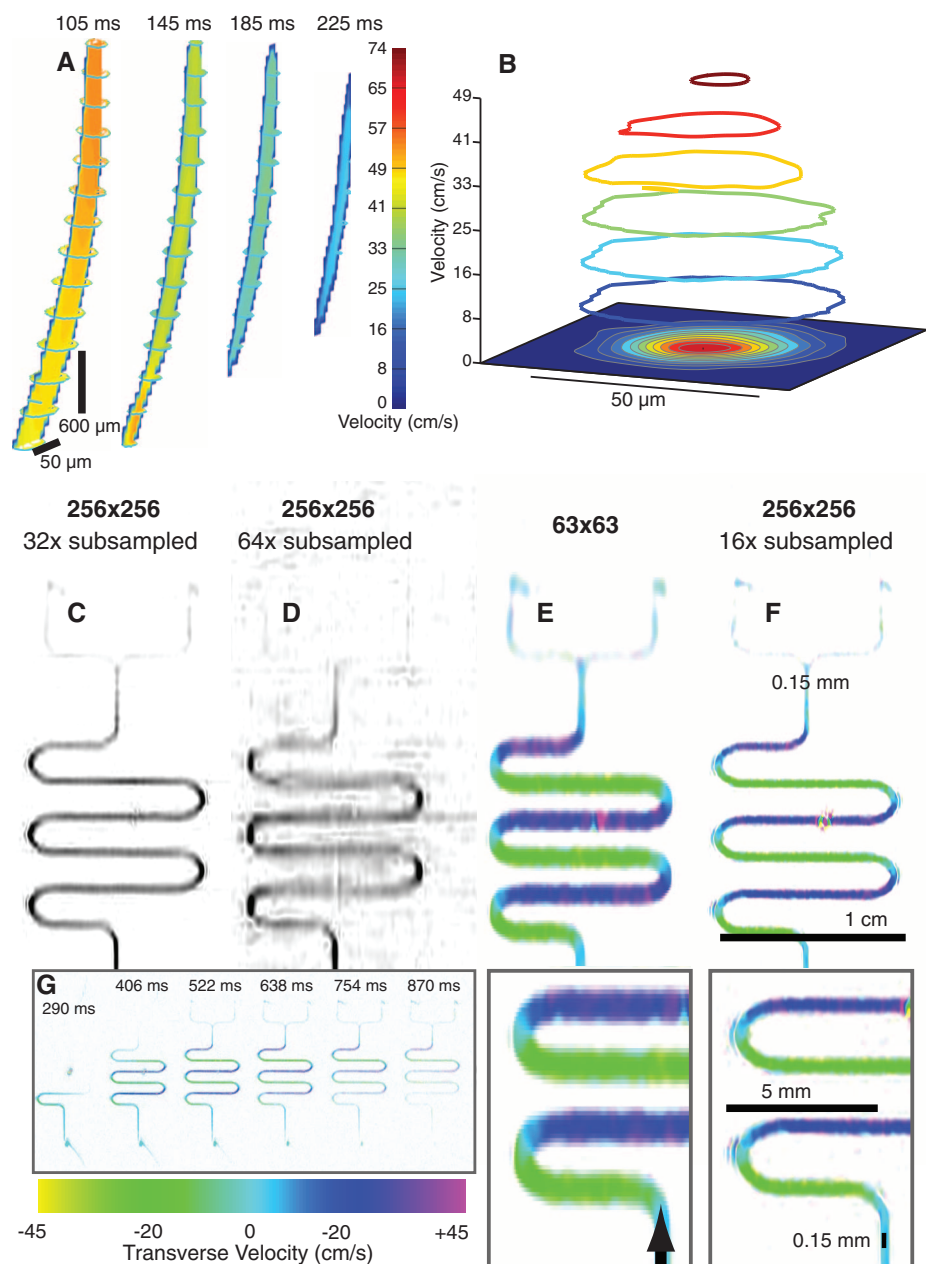
relaxing hyperpolarized substances, such as ^{13}C polarized by dynamic nuclear polarization or optically polarized ^{129}Xe, are used as the encoding medium. Finally, remote detection, in separating the polarization, encoding, and detection steps of an experiment, permits the separate optimization of each. We therefore anticipate that this technol-

ogy, in combination with sensitive NMR chemical sensors (5, 25) and microfabricated NMR detectors (26) based on optical magnetic field sensors that operate at low magnetic fields (27), will be central to the construction of low-cost NMR devices for highly parallel analytical, biomedical, and clinical applications (28).
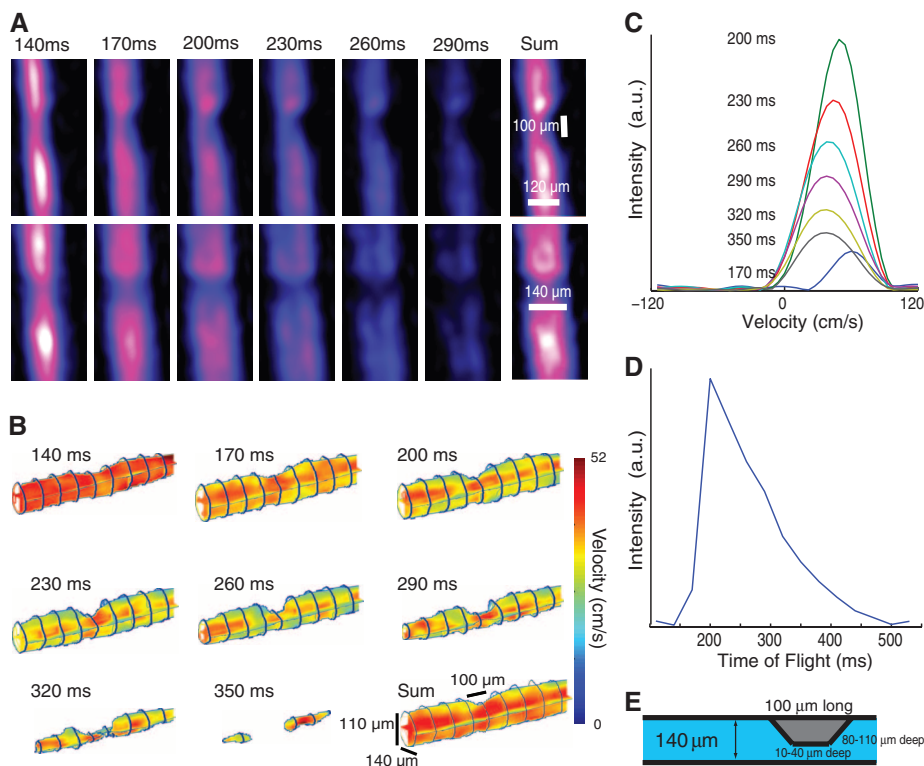

Fig. 2. Images of flow in microfluidic devices. (**A**) Three-dimensional [15 (X) × 15 (Y) × 15 (Z) points] velocity-encoded images of flow through a microcapillary. Each image represents the segments of the flow that arrived with the indicated time of flight (TOF). The 3D contours are drawn at the outer surface of the image (capillary boundary). The colored surface within the 3D capillary indicates the velocity in a plane through the center of the capillary. (**B**) A two-dimensional velocity image cross-section [15 (X) × 15 (Y) points] illustrating parabolic velocity profile in the capillary. (**C** to **G**) Images of flow in a microfluidic serpentine mixer, demonstrating the use of compressed sensing. (C) Image [256 (X) × 256 (Y) pixels] acquired with 32× subsampling. (D) As in (C), but with 64× subsampling. (E) Velocimetric MRI image (63 × 63 pixels) of flow in which the transverse velocity has been encoded. (F) A higher-resolution (256 × 256 pixels) velocimetric image, acquired in the same amount of time as the image in (E) with 16× subsampling. (G) Selected images showing flow pattern as a function of TOF (note: actual time resolution was 50 ms; see movies S1 and S2).

Fig. 3. Accelerating flow in a microfluidic constriction. (**A**) Two-dimensional images (63 × 15 points, *XZ* and *YZ* plane; constriction in *X*) show the high resolution (20 μm) achieved by motion-compensated spatial encoding. The progression reveals fast and slow components of the flow dynamics (see movie S3). The sum is over all TOFs. (**B**) Axial velocity–encoded images [16 (*X*) × 16 (*Y*) × 64 (*Z*)] acquired with 8× subsampling, illustrating acceleration near the constriction and the correlation of velocity and TOF. (**C** and **D**) Around the constriction, flow is dispersive at this spatial resolution; velocity distributions measured at different TOFs (C) reveal fast and slow components, as does the TOF dispersion curve (D). (**E**) Schematic of the constricted microfluidic channel.

References and Notes

1. D. L. Olson, T. L. Peck, A. G. Webb, R. L. Magin, J. V. Sweedler, *Science* **270**, 1967 (1995).
2. Y. Maguire, I. L. Chuang, S. G. Zhang, N. Gershenfeld, *Proc. Natl. Acad. Sci. U.S.A.* **104**, 9198 (2007).
3. C. Massin *et al.*, *J. Magn. Reson.* **164**, 242 (2003).
4. H. Wensink *et al.*, *Lab Chip* **5**, 280 (2005).
5. H. Lee, E. Sun, D. Ham, R. Weissleder, *Nat. Med.* **14**, 869 (2008).
6. Y.-Q. Song, H. Cho, T. Hopper, A. E. Pomerantz, P. Z. Sun, *J. Chem. Phys.* **128**, 052212 (2008).
7. A. J. Moulé *et al.*, *Proc. Natl. Acad. Sci. U.S.A.* **100**, 9122 (2003).
8. J. Jeener, B. H. Meier, P. Bachmann, R. R. Ernst, *J. Chem. Phys.* **71**, 4546 (1979).
9. C. Hilty *et al.*, *Proc. Natl. Acad. Sci. U.S.A.* **102**, 14960 (2005).
10. J. Granwehr *et al.*, *Magn. Reson. Imaging* **25**, 449 (2007).
11. E. Harel, A. Pines, *J. Magn. Reson.* **193**, 199 (2008).
12. E. Fukushima, *Annu. Rev. Fluid Mech.* **31**, 95 (1999).
13. P. T. Callaghan, *Principles of Nuclear Magnetic Resonance Microscopy* (Clarendon, Oxford, 1991).
14. D. G. Cory, A. N. Garroway, *Magn. Reson. Med.* **14**, 435 (1990).
15. M. Lustig, D. Donoho, J. M. Pauly, *Magn. Reson. Med.* **58**, 1182 (2007).
16. D. L. Donoho, *IEEE Trans. Inform. Theory* **52**, 1289 (2006).
17. See supporting material on *Science* Online.
18. J. M. Pope, S. Yao, *Concepts Magn. Reson.* **5**, 281 (1993).
19. G. M. Whitesides, *Nature* **442**, 368 (2006).
20. H. Wu, A. Wheeler, R. N. Zare, *Proc. Natl. Acad. Sci. U.S.A.* **101**, 12809 (2004).
21. C. Monat, P. Domachuk, B. J. Eggleton, *Nat. Photonics* **1**, 106 (2007).
22. S. Koster, E. Verpoorte, *Lab Chip* **7**, 1394 (2007).
23. A. J. deMello, *Nature* **442**, 394 (2006).
24. A. M. Wolters, D. A. Jayawickrama, J. V. Sweedler, *Curr. Opin. Chem. Biol.* **6**, 711 (2002).
25. L. Schröder, T. J. Lowery, C. Hilty, D. E. Wemmer, A. Pines, *Science* **314**, 446 (2006).
26. M. P. Ledbetter *et al.*, *Proc. Natl. Acad. Sci. U.S.A.* **105**, 2286 (2008).
27. J. M. Taylor *et al.*, *Nat. Phys.* **4**, 810 (2008).
28. P. Yager *et al.*, *Nature* **442**, 412 (2006).
29. We thank D. Wemmer for his careful reading of the manuscript and L.-S. Bouchard for helpful discussions. Supported by the U.S. Department of Energy, Office of Basic Energy Sciences, Division of Materials Sciences and Engineering under contract DE-AC02-05CH11231 (V.S.B., J.P., E.H., A.P.). We thank the Agilent Foundation for its generous and unrestricted gift. The Lawrence Berkeley National Laboratory has applied for a patent on aspects of this method. The authors declare no competing interests. Author contributions: V.S.B., J.P., E.H., and A.P. designed the experiments. V.S.B., J.P., and E.H. performed the experiments. V.S.B. and J.P. analyzed the data and wrote the paper.

Probing the Ultimate Limit of Fiber-Optic Strain Sensing

G. Gagliardi,[1]* M. Salza,[1] S. Avino,[1] P. Ferraro,[1] P. De Natale[2]

The measurement of relative displacements and deformations is important in many fields such as structural engineering, aerospace, geophysics, and nanotechnology. Optical-fiber sensors have become key tools for strain measurements, with sensitivity limits ranging between 10^{-9} and $10^{-6}\varepsilon$ hertz (Hz)$^{-1/2}$ (where ε is the fractional length change). We report on strain measurements at the $10^{-13}\varepsilon$-Hz$^{-1/2}$ level using a fiber Bragg-grating resonator with a diode-laser source that is stabilized against a quartz-disciplined optical frequency comb, thus approaching detection limits set by thermodynamic phase fluctuations in the fiber. This scheme may provide a route to a new generation of strain sensors that is entirely based on fiber-optic systems, which are aimed at measuring fundamental physical quantities; for example, in gyroscopes, accelerometers, and gravity experiments.

Optical sensors and interferometers are widely used for high-sensitivity strain measurements. Gravitational-wave, long-baseline interferometers are the most sensitive strain detectors developed to date, with impressively low detection limits on the order of $10^{-22}\varepsilon$ Hz$^{-1/2}$ (where ε is the fractional length change), from a few tens of hertz up to the kilohertz range (*1*).

However, these detectors are extremely complex and cumbersome, with a length of several kilometers. Smaller–length scale (centimeter) optical-fiber sensors are widespread tools for static and dynamic local-deformation monitoring inside mechanical structures and materials, in environments as diverse as ocean depths, geothermal wells (*2*), and aircrafts (*3*). Strain sensitivities ranging between 10^{-9} and $10^{-6}\varepsilon$ Hz$^{-1/2}$ are presently feasible with the use of standard telecommunication fiber technology (*4*). Higher strain resolutions have been demonstrated with passive fiber-optic resonators using frequency-stabilized lasers (*5, 6*)

[1]Consiglio Nazionale delle Ricerche–Istituto Nazionale di Ottica (INO) and European Laboratory for Non-Linear Spectroscopy (LENS), Comprensorio "A. Olivetti," Via Campi Flegrei 34, I-80078 Pozzuoli (Naples), Italy. [2]Consiglio Nazionale delle Ricerche–INO and LENS, Largo E. Fermi 6, I-50125 Firenze, Italy.

*To whom the correspondence should be addressed. E-mail: gianluca.gagliardi@ino.it